



Multi-interfacial microbubbles controlled sequential cavitation for synergistic vascular destruction/chemotherapeutic therapy

Tiandong Chen^a, Chenyi Zhang^a, Yanxiao Zhao^a, Yakun Wang^a, Mingxi Li^a, Yang Liu^a, Xiao Wang^a, Shuangyu Liu^a, Dan Mu^{b,*}, Fang Yang^{a,*}

^a State Key Laboratory of Digital Medical Engineering, School of Biological Science and Medical Engineering, Southeast University, Nanjing 211189, PR China

^b Department of Radiology, Shanghai Tenth People's Hospital, Tongji University School of Medicine, Shanghai 200072, PR China

ARTICLE INFO

Keywords:

Multi-interfacial microbubbles
Sequential cavitation
Vascular destruction
Deep penetration

ABSTRACT

Microbubbles have emerged as versatile theranostic platforms in biomedicine. In addition to being used as ultrasound contrast agents, capitalizing on cavitation-mediated physical effects, microbubbles now enable targeted drug delivery and precision tumor ablation. In this study, we engineer doxorubicin (DOX)-loaded multi-interfacial microbubbles (DOX-MIMBs) through interfacial self-assembly of hydrophobic mesoporous silica nanoparticles (hMSNs), establishing a hierarchically structured MIMBs with the sustained acoustic activity. Strong affinity between hMSNs and the gas-liquid interface facilitates cavitation effect transmission. Under low intensity ultrasound ($<3 \text{ W/cm}^2$) irradiation, primary MIMBs collapse generates secondary daughter bubbles that rapidly stabilize via hMSNs-mediated gas-liquid interface reconstruction and are able to cavitate again. This process enables energy-cascaded cavitation-successive bubble generations persisting until acoustic energy dissipation, achieving prolonged cavitation duration *versus* conventional lipid-shelled microbubbles. The sequential acoustomechanical perturbation generated by DOX-MIMBs induced synergistic tumor therapy: selective vascular destruction for mechanically collapsed immature tumor vasculature and enhanced chemotherapy for wider distribution and deeper penetration of DOX in tumors. Utilizing sequential bubble cavitation-induced shockwave and microstreaming, by integrating tumor vasculature mechanical disruption and deep tumor DOX penetration chemotherapy, DOX-MIMBs achieved tumor volume appropriate 90 % reduction in renal cell carcinoma models. Such elaborated DOX-MIMBs mechano-pharmaceutical delivery system achieve a paradigm shift from systemic drug bombardment to local mechanochemical tumor suppression and provide a powerful strategy for tumor precision therapy.

1. Introduction

Renal cell carcinoma (RCC) is one of the most common and deadly malignant tumors in the kidney, accounting for approximately 90 % of renal cancers [1–3]. Renal cell carcinoma is a highly vascularized malignant tumor, and angiogenesis plays a key role in its progression and metastasis [4,5]. Despite the clinical success of anti-angiogenic agents such as vascular endothelial growth factor inhibitors, their long-term efficacy is limited by drug resistance, adverse side effects and incomplete tumor response [6,7]. Therefore, new and innovative approaches to inhibit angiogenesis and improve therapeutic efficacy are urgently needed.

Given that tumor growth and progression are dependent on neovascularization, inhibition of angiogenesis by non-invasive physical

methods may be a novel strategy to suppress RCC [8,9]. Ultrasound-mediated microbubble cavitation (UMC) has attracted much attention due to its non-invasive, localized action and potential for precise disruption of tumor vasculature [10,11]. Microbubbles are gas-filled vesicles with lipid, protein, or polymer shells that oscillate and collapse under ultrasound irradiation. Disruption or cavitation of microbubbles can generate mechanical forces to induce vascular endothelial damage, transient vasoconstriction, and thrombosis [12,13]. Preclinical studies on other solid tumors, such as hepatocellular carcinoma and glioblastoma, have demonstrated that UMC effectively reduces tumor perfusion and mechanically disrupts immature tumor vessels and downregulates vascular endothelial growth factor [14,15]. Importantly, this mechanical disruption circumvents molecular resistance mechanisms of antiangiogenic drugs. However, the instability of

* Corresponding authors.

E-mail addresses: mudan118@126.com (D. Mu), yangfang2080@seu.edu.cn (F. Yang).

<https://doi.org/10.1016/j.jconrel.2025.114287>

Received 31 July 2025; Received in revised form 26 September 2025; Accepted 30 September 2025

Available online 1 October 2025

0168-3659/© 2025 Elsevier B.V. All rights reserved, including those for text and data mining, AI training, and similar technologies.

traditional lipid-shelled microbubbles often leads to poor cavitation and drug leakage.

The exceptional longevity and stability of interfacial bubbles has been widely accepted and has fascinated researchers [16–18]. While the stability of conventional shelled microbubbles depends on the shell material (phospholipids, polymers, and albumin) [19–21], the presence of interfacial bubbles depends on the substrate. Although the mechanism of interfacial bubble formation is uncertain, there is growing evidence that contact line pins on the substrate are necessary for the presence of interfacial bubbles [22]. In addition, the hydrophobicity of the solid substrate contributes to the formation of interfacial bubbles [23]. A few attempts have been made to use interfacial bubbles for tumor therapy [24–26]. However, these interfacial bubbles are limited by particle size, which produces undesirable bubble cavitation and very limited vascular destruction.

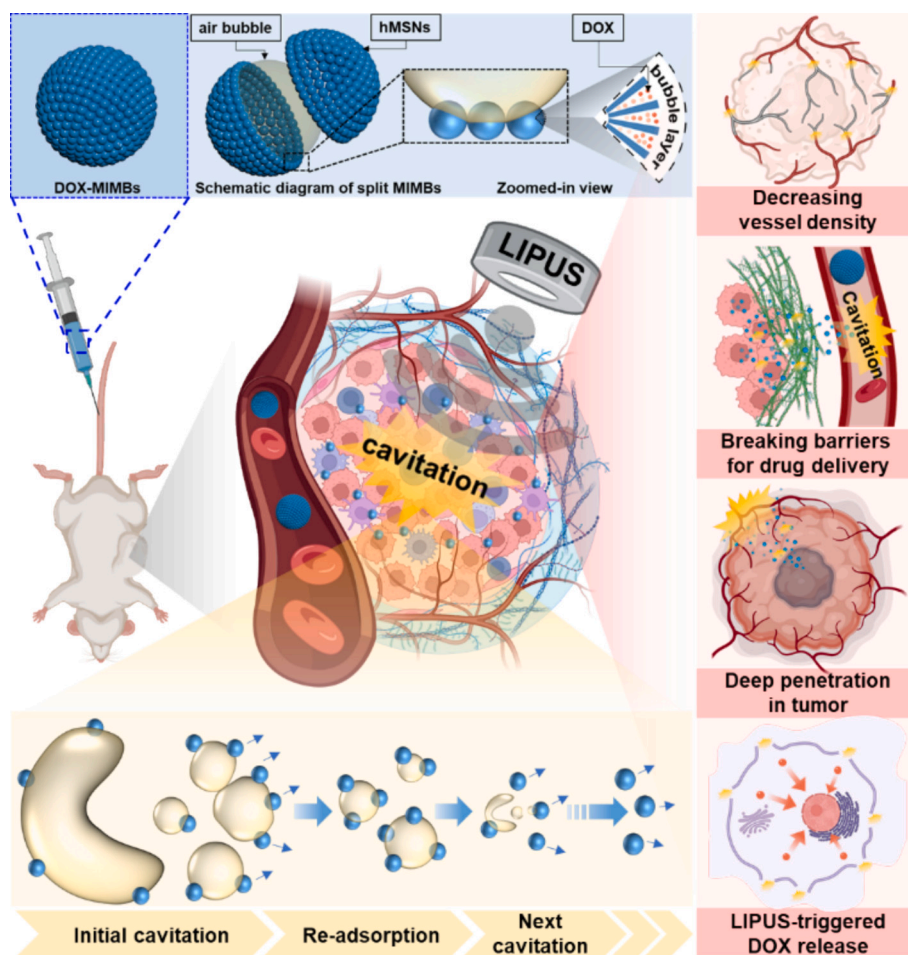
In this study, a novel sequential cavitation therapeutic platform, multi-interfacial microbubbles (MIMBs), is proposed. MIMBs are curved substrate-stabilized bubbles assembled from multiple hydrophobic mesoporous silica nanoparticles (hMSNs). Moreover, DOX, as a broad-spectrum antitumor drug [27–29], was selected and loaded into the hydrophobic mesopores of hMSNs to prepare DOX-loaded MIMBs (DOX-MIMBs) for acoustically triggered sequential cavitation enhanced drug penetration. Due to their interfacial bubble nature, MIMBs exhibit enhanced stability, which facilitates the reduction of drug leakage during blood circulation. As shown in Scheme 1, under low-intensity pulsed ultrasound (LIPUS), DOX-MIMBs produce daughter bubbles after initial cavitation, which are rapidly re-stabilized by hMSNs,

resulting in sequential bubble cavitation. Such spatiotemporally controlled cavitation exerts dual mechano-pharmaceutical actions: i) Vascular destruction: Sequential inertial cavitation induces tumor vessel pruning to form blood clots in tumor vessels and blocking tumor blood perfusion; ii) Enhanced chemotherapy: Sequential cavitation breaks barriers to enhance DOX extravasation, achieving deeper intratumoral penetration than the enhanced permeability and retention (EPR)-mediated passive delivery. Therefore, such hierarchically engineered MIMBs can integrate physical and pharmacological modalities to achieve a paradigm shift from systemic drug bombardment to local mechanochemical tumor suppression.

2. Materials and methods

2.1. Materials

MSNs (140–180 nm) were brought from Nanjing XFNANO Materials Tech Co., Ltd. (China). Doxorubicin (DOX), FITC-dextran (70 kDa) and hexamethyldisilazane (HMDS) were purchased from Shanghai Maclean Biochemical Technology Co., Ltd. The SonoVue, commercial microbubbles, was obtained from Bracco (Milan, Italy). 1, 1'-dioctadecyl-3, 3', 3'-tetramethylindocarbocyanine perchlorate (DiI) was provided by KeyGEN BioTECH (Nanjing, China). Rabbit monoclonal anti-CD34 antibody (ab316277) was purchased from Abcam (Cambridge, United Kingdom).



Scheme 1. Schematic illustration of the structure of DOX-MIMBs and their cavitation for vascular destruction and chemotherapy (Created with BioRender.com). Under LIPUS, sequential MIMBs cavitation occurred to collapse the immature tumor vasculature and break barriers for deeper DOX penetration. Meanwhile, sequential cavitation-induced mechanical damage and DOX release achieved enhanced the tumor inhibitory efficacy.

2.2. Synthesis of hydrophobic MSNs (hMSNs)

hMSNs were prepared using the method in the previous publication [30]. In brief, 50 mg of MSNs were added in 8 mL ethanol. After bath sonication, 2 mL of HMDS was added. The mixture was stirred at 50 °C for 42 h. After cooling to room temperature (25 °C), the mixture was centrifuged (9500 ×g, 8 min) to collect the precipitate. After washed with ethanol twice, hMSNs were obtained by vacuum drying at 60 °C overnight.

2.3. Preparation of MIMBs

In a 3 mL vial, hMSNs were mixed with 1 mL of saline. The vial was corked with a rubber stopper and sealed with an aluminium cap. Then, the vial was shaken at 70 Hz for 6 min in a tissue homogenizer (Xianou-48, ATPIO, China) to generate MIMBs.

2.4. Preparation of DOX-loaded MIMBs

DOX-loaded MIMBs (DOX-MIMBs) were prepared according to previous report with some modification [31]. Briefly, 5 mg of hMSNs and 5 mg of DOX were suspended in 1 mL 75 % ethanol solution. After stirring for 2 h, the ethanol was vaporized at 60 °C, and the process was repeated three times by adding ethanol. Free DOX was removed by washing with water. DOX-loaded hMSNs were collected by centrifugation at 9500 ×g for 8 min. 3 mg of DOX-loaded hMSNs and 1 mL of saline were added into a 3 mL vial. The vial was corked with a rubber stopper and sealed with an aluminium cap. The vial was shaken at 70 Hz for 6 min to generate DOX-MIMBs.

The drug loading content (DLC) and the drug loading efficiency (DLE) of DOX were measured by UV-vis spectroscopy and calculated using the following eq. (1) and (2):

$$DLC\% = \frac{\text{weight of loaded DOX}}{\text{total weight of DOX - MIMBs}} \times 100\% \quad (1)$$

$$DLE\% = \frac{\text{weight of loaded DOX}}{\text{weight of feeding DOX}} \times 100\% \quad (2)$$

2.5. Structure characterization

The size distribution was measured using dynamic light scattering (DLS) on a Zeta-Sizer Nano-ZS 90 (Malvern Instruments, UK). The bubble concentration was measured by a coulter particle counting and particle size analyzer (Multisizer 4e, USA). Morphologies of MIMBs were obtained using a scanning electron microscope (SEM) on an Ultra Plus instrument (Zeiss, Germany) and a confocal microscope (Olympus, TIC2 plus, Japan).

2.6. Ultrasound imaging in vitro

In vitro ultrasound imaging was conducted on a high-resolution microimaging system (VisualSonics Vevo 2100, Canada) on linear mode (B-mode) and non-linear mode (Contrast-mode). MIMBs with different concentrations were added into tissue-mimicking agarose phantoms for ultrasound imaging. The parameters for contrast-mode were set as follow: power 20 %, frequency 18 MHz, contrast gain 35 dB. The parameters for B-mode were set as follow: power 20 %, frequency 18 MHz, 2D gain 18 dB. These parameters are applied in all *in vitro* ultrasound imaging unless otherwise noted.

2.7. Stability of MIMBs

During blood circulation, MIMBs may suffer from low pressure. During inhalation, the diaphragm contracts and the chest expands, causing the right atrial pressure, which is close to 0 mmHg, to further

decrease to a negative value [32,33]. To simulate the effect of low pressure on MIMBs, MIMBs or SonoVue were diluted to 1.0×10^7 per mL with saline, added in a vial, and placed in a negative pressure environment (−10 mmHg) for 30 min. Ultrasound imaging was performed to record the ultrasound signal changes.

To evaluate the effect of pH values on MIMBs, MIMBs or SonoVue were diluted to 1.0×10^7 per mL with phosphate buffer (pH = 7.4, 6.5, and 6.0) or acetate buffer solution (pH = 5.5 and 5.0). Ultrasound imaging was performed to record the ultrasound signal changes.

To evaluate the effect of surfactants on MIMBs, sodium dodecyl sulfate (SDS) solution was mixed with MIMBs or SonoVue to make a final SDS concentration of 1, 2, and 4 mg/mL. Ultrasound imaging was used to monitor the changes in the ultrasound signal.

The storage stability was evaluated by storing freshly prepared MIMBs at 25 °C for 1, 2, 4, 8, and 16 days. Throughout this period, ultrasound imaging was used to monitor the changes in the ultrasound signal.

2.8. Ultrasound treatment

An ultrasonic therapy instrument (DM-200B, Dimip, China) was used to produce pulsed ultrasound. The parameters of pulsed ultrasound were as follows: frequency 1 MHz, pulse repetition frequency 100 Hz, intensity 0.25–3 W/cm². Pulsed ultrasound with intensity <3 W/cm² is considered as low-intensity pulsed ultrasound [34]. LIPUS was transmitted to bubble samples through water or agarose gel, to cells through culture medium, and to tissues (kidney and tumor) through commercial ultrasonic coupling (HYNAUT, China).

2.9. Measurement of LIPUS thermal effect

10 mL of saline in a plastic tube was contacted with the transducer of LIPUS through commercial ultrasonic coupling. The temperature probe was inserted in saline. The temperature was recorded every ten seconds during LIPUS treatment. LIPUS power was set as: 0.25, 0.5, 1, 1.5, and 2 W/cm².

2.10. Drug release

DOX-MIMBs were added to a dialysis tube (Mw 2000). The dialysis tube was immersed in 20 mL saline. At the predetermined time points (1, 2, 3, 4, 5, 6, 7, 8, 9, 10 and 24 h), 5 mL of saline was removed to measure DOX amount, and 5 mL fresh saline was supplemented. At the 5 h, DOX-MIMBs in the dialysis tube were treated by LIPUS (0.25, 0.5, and 1 W/cm², 20 s).

2.11. Cell culture

Mouse renal carcinoma (Renca) cells and human umbilical vein endothelial cells (HUVECs) were provided by Procell Life Science & Technology Co., Ltd., and cultured in Dulbecco's modified Eagle's medium (DMEM) supplemented with 10 % FBS, 100 U/mL penicillin, and 100 µg/mL streptomycin in a humidified atmosphere consisting of 5 % CO₂ and 95 % air at 37 °C.

2.12. Cell viability

Renca cells or HUVECs were seeded in 96-well plates with the density of 8000 cells/well and incubated overnight. Cells were treated with different concentration of free DOX and DOX-MIMBs with or without LIPUS (0.25 W/cm², 20 s) treatment. After incubation for 24 h, 10 µL of CCK-8 solution was added. After incubation for another 2 h at 37 °C, cell viability was evaluated by absorbance at 450 nm measured on a microplate reader (Multiskan Sky, Thermo Fisher Scientific, USA). Cell viability (%) was determined as following eq. (3):

$$\text{Cell viability}\% = \frac{\text{OD}_{\text{sample}} - \text{OD}_{\text{blank}}}{\text{OD}_{\text{control}} - \text{OD}_{\text{blank}}} \times 100\% \quad (3)$$

Samples are cells treated with MIMBs, free DOX, or DOX-MIMBs; control groups are cells treated with DMEM medium; blank groups are medium alone.

To the suspension of Renca cells or HUVECs, SonoVue or MIMBs (the same particle concentration) were added and treated by LIPUS (0.25 W/cm², 20 s). Then, cell viability was measured by CCK-8 method.

Renca cells were treated by LIPUS (0.25 W/cm², 20 s) with or without SonoVue or MIMBs. Then, cells were stained with Trypan blue. Trypan blue positive cells were counted by an automated cell counter (Invitrogen, USA).

2.13. Internalization of MIMBs and DOX-MIMBs

To prepare DiI-labeled MIMBs (DiI-MIMBs), 10 mg of hMSNs were dispersed in 1 mL of DiI ethanol solution (1 mg/mL). After stirring for 4 h at room temperature, DiI-labeled hMSNs were collected by centrifugation (8 °C, 9500 ×g, 8 min) and drying at 60 °C overnight. DiI-labeled hMSNs were used to prepare DiI-MIMBs.

To analyze time-dependent cellular uptake, Renca cells were seeded and incubated overnight. Cells were treated with DiI-MIMBs and incubated for 0.5, 1, 2, and 4 h. Cells were imaged by a confocal laser scanning microscopy (Olympus, TIC2 plus, Japan) after nuclei were stained with DAPI, or collected and analyzed by flow cytometry (ThermoFisher, Attune NxT, USA).

To observe intracellular distribution of MIMBs, Renca cells were seeded in glass-bottom plates and incubated overnight. Cells were treated with DiI-MIMBs and incubated for 1 h. Next, cells were treated by LIPUS (0.25 W/cm², 20 s). Cells were washed with PBS for three times. Nuclei were stained with Hoechst 33342, and endosomes/lysosomes were labeled by LysoTracker™ Green DND-26. Cells were imaged to visualize the distribution of DiI-MIMBs.

To observe sequential cavitation in cells, Renca cells were seeded in a glass-bottom plate and incubated overnight. DiI-MIMBs were added to the plate. Then the plate was sealed and placed upside down. After incubation for 0.5 h, cells were washed and fixed with 4 % polyformaldehyde. Nuclei were stained with DAPI. Cells were observed by the confocal laser scanning microscopy before and after LIPUS (0.25 W/cm², 20 s) treatment.

To analyze DOX amount in cells, Renca cells were seeded and incubated overnight. Free DOX or DOX-MIMBs (20 µg/mL DOX) were added, and cells were treated with LIPUS (0.25 W/cm², 20 s). Cells were washed, collected and analyzed by flow cytometry.

To observe DOX release in cells, Renca cells were seeded in glass-bottom plates and incubated overnight. Cells were treated with free DOX and DOX-MIMBs (20 µg/mL DOX) and incubated for 2 h. Cells were washed and imaged by a confocal laser scanning microscopy. In another plate, cells were treated with DOX-MIMBs and incubated for 1 h. Then, cells were treated by LIPUS (0.25 W/cm², 20 s). After incubation for another 20 min or 60 min, cells were washed and imaged by a confocal laser scanning microscopy.

2.14. Animal models

Male BALB/c nude mice (18–20 g) were purchased from Wukong Biotechnology (Nanjing, China) and bred in an experimental animal room of SPF grade. Distilled water and sterile food were provided to all mice. Animals were acclimatized to their new environment for 7 days prior to treatment. All animal experiments, animal care, and animal model protocols were approved by the Committee on the Ethics of Animal Experiments of the Institute of Process Engineering at the Southeast University (NO. 20230303001). Male BALB/c nude mice were subcutaneously injected at the right thigh with 100 µL of fetal bovine serum containing 5×10^6 Renca cells.

2.15. Color Doppler imaging

Blood flow of tumors or kidneys was detected by color Doppler imaging on a high-resolution microimaging system (VisualSonics Vevo 2100, Canada). The imaging parameters were as follows: power 100 %, frequency 16 MHz. Area of blood flow that can be detected as a percentage of the total ROI was calculated by ImageJ software.

2.16. Ultrasound imaging in vivo

50 µL of MIMBs were injected intravenously in tumor-bearing mice. Ultrasound imaging was performed immediately to observe tumors. The imaging parameters for contrast-mode were as follows: power 20 %, frequency 18 MHz, contrast gain 35 dB.

2.17. Tumor penetration in vitro and in vivo

Renca 3D tumor spheroids were established according to the previous method [35]. Renca cells were seeded in a 96-well plate pretreated with agarose gel (1.5 % w/v). After 4 days of incubation, Renca 3D tumor spheroids were established. Free DOX, free DOX + SonoVue and DOX-MIMBs were added. DOX concentration of all groups was set as 20 µg/mL. Renca 3D tumor spheroids were treated immediately with LIPUS (0.25 W/cm², 20 s). Next, Renca 3D tumor spheroids were transferred to clean wells and washed with PBS for three times. Renca 3D tumor spheroids were imaged by a confocal laser scanning microscopy (Olympus, TIC2 plus, Japan).

To visualize tumor penetration *in vivo*, SonoVue was labeled with DiI. Briefly, 50 µL of ethanol solution (1 mg/mL) was mixed with 1 mL of SonoVue suspension. After incubation at room temperature for 10 min, the suspension was centrifuged (50 ×g, 2 min) and redispersed in saline.

Free DiI, DiI-SonoVue (4.0×10^7 bubbles) and DiI-MIMBs (4.0×10^7 bubbles) were injected intravenously in tumor-bearing mice, respectively. Tumors were immediately treated with LIPUS (2 W/cm², 1 min). Mice were sacrificed and tumors were collected for analyze the distribution of DiI in tumor tissues.

2.18. Biosafety

DiI-SonoVue (4.0×10^7 bubbles) or DiI-MIMBs (4.0×10^7 bubbles) were injected intravenously in BALB/c mice. Right kidneys were immediately treated with LIPUS (2 W/cm², 1 min). Kidney blood perfusion was detected by color Doppler imaging. After mice were executed, kidneys were collected and imaged by an imaging system (AniView 600, China).

100 µL of FITC-dextran saline solution (10 mg/mL) was injected in BALB/c mice *via* tail vein. Then SonoVue (4.0×10^7 bubbles) or MIMBs (4.0×10^7 bubbles) were injected intravenously. Right kidneys were immediately treated with LIPUS (2 W/cm², 1 min). After mice were executed, kidneys were collected and fixed with 4 % polyformaldehyde for histological evaluation.

2.19. Tumor accumulation

Male Balb/c nude mice were injected subcutaneously with Renca cells in the right thigh and randomized to two groups ($n = 3$): DiI-MIMBs and DiI-MIMBs+LIPUS. After 2 weeks, mice were given intravenous injection of 200 µL of DiI-MIMBs. Meanwhile, the tumor was treated immediately by LIPUS (2 W/cm², 1 min). Mice were imaged and analyzed using an IVIS spectrum imaging system (Caliper, USA) at different time points.

2.20. In vivo tumor therapy

Male Balb/c nude mice were injected subcutaneously with Renca cells in the right thigh on day 0 and randomized to four groups ($n = 5$):

saline, MIMBs+LIPUS, DOX-MIMBs and DOX-MIMBs+LIPUS. Mice were given intravenous injection of MIMBs or DOX-MIMBs (3 mg/kg DOX), and treated immediately by LIPUS (2 W/cm², 1 min) on day 7, 11, 15 and 19. The tumor volume and body weight of the mice were measured every 2 days according to eq. (4):

$$\text{Tumor volume} = \frac{\text{length} \times \text{width}^2}{2} \quad (4)$$

Euthanasia was performed on day 28, and tumors and major organs were collected for histological evaluation.

2.21. Histopathological evaluation

DiI-SonoVue (4.0 × 10⁷ bubbles) and DiI-MIMBs (4.0 × 10⁷ bubbles) were injected intravenously in tumor-bearing mice, respectively. Tumors were immediately treated with LIPUS (2 W/cm², 1 min). Mice were executed. Tumors were collected and fixed with 4 % polyformaldehyde

for histological evaluation.

For histological evaluation, tumors and kidneys were embedded in paraffin and sectioned. H&E and CD34 staining were performed for kidneys. H&E, TUNEL, Ki67 and CD34 staining were performed for tumors. The vessel density was quantified as the percentage of CD34-positive area to total area.

2.22. Statistical analysis

Quantitative data were presented as means ± standard deviation (SD) from sample numbers (n). Data from experiments were analyzed using Origin 2022. Statistical comparisons were made by unpaired Student's *t*-test (between two groups). *P* value <0.05 was considered statistically significant.

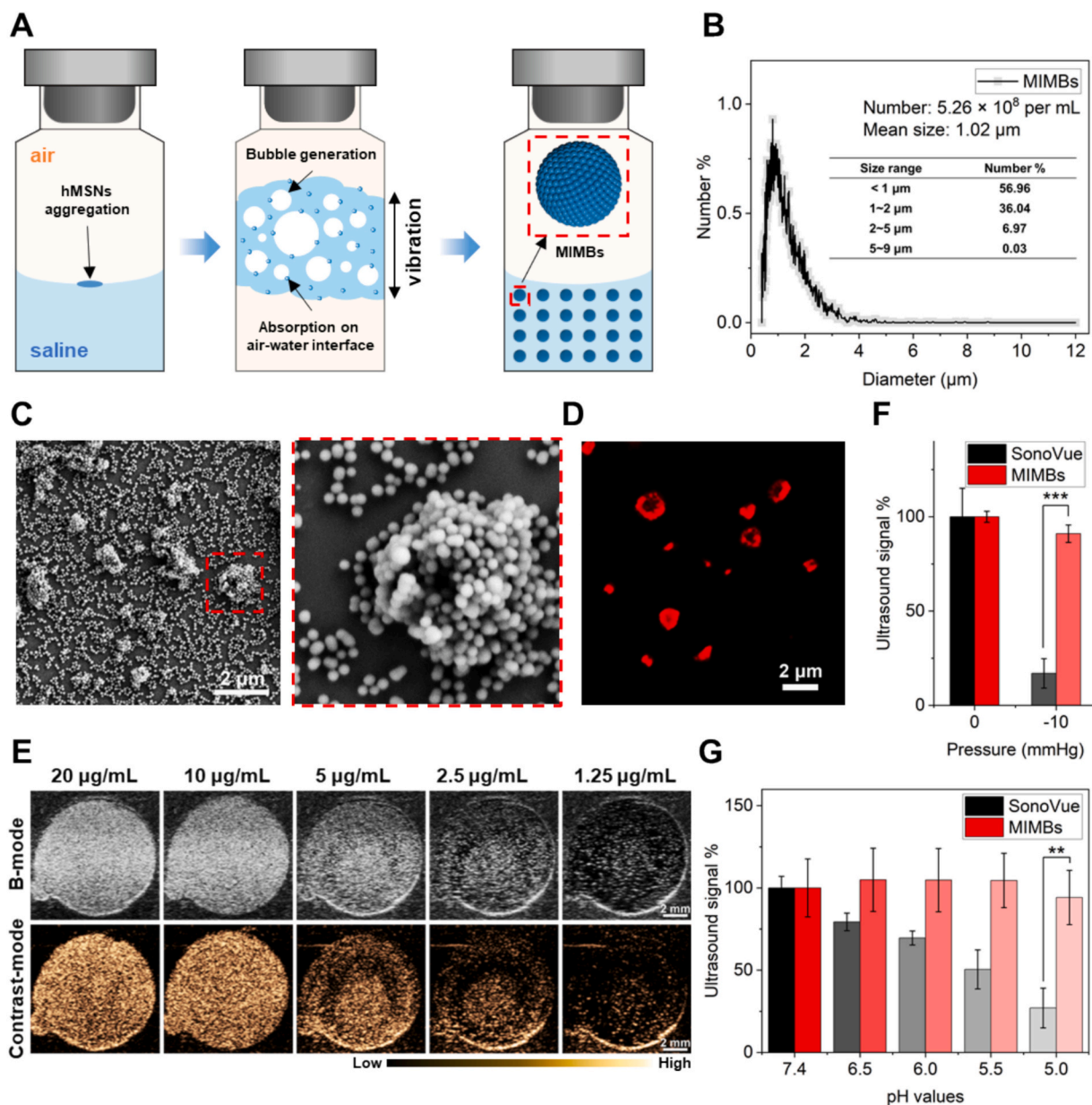


Fig. 1. (A) Schematic diagram of the procedure of preparing MIMBs. (B) MIMBs counting and size. (C) SEM image of MIMBs. (D) Fluorescent image of DiI-MIMBs. (E) Images of MIMBs in contrast-enhanced ultrasound imaging at different concentrations. (F) Quenching effect of the ultrasound response of MIMBs under vacuum (−10 mmHg) for 30 min. (G) Ultrasound signal changes of MIMBs at different pH values. ***P* < 0.01, ****P* < 0.001.

3. Results and discussion

3.1. Preparation and characterization of MIMBs

MIMBs were prepared by vibration. As depicted in Fig. 1A, hMSNs were mixed with air and saline in a sealed vial. During violent vibration, large air bubbles were initially produced. Then, hMSNs rapidly absorbed onto the gas-water interface of large bubbles to produce hMSNs-stabilized foam or large bubbles (tens of micrometers) (Fig. S1). With further violent shaking, the size of these hMSNs-stabilized foam and large bubbles decreased and MIMBs were generated. The average size of MIMBs was measured to be $1.02\ \mu\text{m}$ with number concentration of 5.26×10^8 per mL (1 mg/mL hMSNs) (Fig. 1B). MIMBs exhibited hollow structures with hMSNs assembled on the shell (Fig. 1C, D). The unique structure of MIMBs imparts excellent acoustic scattering characteristics. As shown in Fig. 1E, MIMBs exhibited concentration-dependent contrast ability in both B-mode and Contrast-mode ultrasound imaging. Even at very low concentrations ($<20\ \mu\text{g/mL}$), MIMBs exhibited excellent ultrasonic contrast.

The stability of MIMBs is essential for vascular destruction and drug delivery. Freshly prepared MIMBs were stored at $25\ ^\circ\text{C}$ for varying durations. The ultrasound signal intensity decreased by less than 10 % within the first 4 days but showed a notable decrease of 32.6 % after 16 days (Fig. S2), suggesting that MIMBs maintained good stability over the shorter period. To further investigate their stability, the MIMBs were subjected to a range of different conditions. After MIMBs were injected into vessels, MIMBs suffered from venous low pressure. As shown in Fig. 1F, contrast enhancement of MIMBs in ultrasound imaging was only reduced by 9.0 % at $-10\ \text{mmHg}$ pressure, while that of SonoVue (commercial microbubbles in clinical use) was reduced by 83.0 %. Lower ambient pressure leads to a decrease in the solubility of the gas in the water according to Henry's Law. This disrupts the equilibrium between the gases in SonoVue and the dissolved gases in water, causing the gases to escape from SonoVue and ultimately leading to a rapid decrease in ultrasonic signal. However, the hydrophobic substrate consisting of hMSNs in MIMBs can greatly prevent gas from escaping. This is because gases tend to accumulate near the hydrophobic interface [36], causing this equilibrium to be less susceptible to ambient pressure.

When MIMBs reached tumor tissue, the weak acidic microenvironment ($\text{pH} = 6.5\text{--}5.0$) of tumor tissue may have an effect on their stability. Thus, the effect of pH value *in vitro* on MIMBs structure was investigated. As shown in Fig. 1G, contrast enhancement of SonoVue in ultrasound imaging gradually reduced with decrease of pH values. Interestingly, MIMBs were virtually unaffected by the change of environmental pH. In specific, contrast enhancement of MIMBs in ultrasound imaging was not reduced at pH 6.5, 6.0, and 5.5. It was only reduced by 5.8 % at pH 5.0, while that of SonoVue was reduced by 73.0 % at pH 5.0. Different from conventional gas-encapsulated bubbles that depend on the shell materials for their stability, the stability of MIMBs depends on hMSNs hydrophobicity that is barely affected by acidic environment.

Surfactants such as SDS can render hydrophobic surfaces hydrophilic and thus significantly disrupt the structure of interfacial microbubbles. As shown in Fig. S3, the ultrasound signal enhancement of SonoVue was reduced by 85.3 % in the presence of 1 mg/mL SDS and disappeared completely at 4 mg/mL. This is attributed to the ability of SDS to solubilize phospholipid shells, leading to gradual bubble disruption with increasing concentration. In contrast, the ultrasound signal of MIMBs decreased by 69.9 % at 1 mg/mL SDS but remained unchanged upon further SDS addition. We speculated that this phenomenon may be related to the presence of interfacial nanobubbles. Previous studies have indicated that the effect of SDS on interfacial bubbles diminished with decreasing bubble size and becomes negligible for nanobubbles [37,38].

3.2. LIPUS-mediated MIMBs internalization

In order to determine an appropriate ultrasound intensity for cellular

experiments, HUVECs were treated with LIPUS for 20 s and immediately stained with Trypan blue (a dye to detect cell membrane integrity). As shown in Fig. S4, Trypan blue positivity cells were 12.3 %, 78.3 %, and 96.3 % induced by 0.25, 0.5 and $1\ \text{W/cm}^2$, respectively. Therefore, LIPUS with $0.25\ \text{W/cm}^2$ was used in the following cellular experiments.

MIMBs were internalized by Renca cells in a time-dependent manner. With longer incubation time, more DiI-labeled MIMBs (DiI-MIMBs) were internalized (Fig. 2A, B). As shown in Fig. 2C, internalized DiI-MIMBs (red) co-localized with endosomes/lysosomes (green) (white triangles). Interestingly, under LIPUS ($0.25\ \text{W/cm}^2$, 20 s) treatment, more DiI-MIMBs entered the cytoplasm and did not co-localize with endosomes/lysosomes (white arrows). These results showed that LIPUS promoted the intracellular accumulation and endosomal/lysosomal escape of MIMBs, evidenced by the decreased Pearson correlation coefficient (Fig. S5). Under LIPUS, MIMBs cavitation occurred and generated shock waves to disrupt cell membranes. After LIPUS treatment, MIMBs cavitation occurred in the vicinity of fixed cells and promoted direct entry of MIMBs into the cytoplasm independent of cellular activity (Fig. 2D). This also highlighted the potential of MIMBs cavitation to break through drug delivery barriers.

As indicated by Trypan blue staining, Trypan blue positive rate of MIMBs+LIPUS was 2.0 times that of SonoVue+LIPUS (Fig. 2E), indicating stronger MIMBs cavitation than SonoVue at the same particle concentration. Disruption of cell membranes also induced cell death. MIMBs alone exhibited almost no cytotoxicity at concentrations below $800\ \mu\text{g/mL}$ (Fig. S6). However, cell viability of Renca and HUVECs cells induced by MIMBs+LIPUS was reduced from 96.4 % to 43.6 % and 98.3 % to 34.9 %, respectively (Fig. 2F), demonstrating potential antitumor and vascular destruction efficacy.

3.3. LIPUS-mediated drug release

To enhance the anti-tumor effect, DOX-loaded MIMBs (DOX-MIMBs) were prepared. DLC of DOX in DOX-MIMBs was calculated to be 8.4 %, and DLE was 16.8 %. DOX release profile was recorded and shown in Fig. 3A. Without LIPUS treatment, the cumulative release of DOX from DOX-MIMBs within 5 h was less than 14 %. Interestingly, after LIPUS ($0.25\ \text{W/cm}^2$, 20 s) treatment, the cumulative release of DOX within the next 5 h was 67.2 %. And that is 76.8 % after LIPUS ($0.5\ \text{W/cm}^2$, 20 s) treatment and 85.3 % after LIPUS ($1\ \text{W/cm}^2$, 20 s) treatment. LIPUS treatment extremely accelerated DOX release from DOX-MIMBs. A hypothesis was proposed to explain LIPUS-triggered drug release. As depicted in Fig. 3B, the hydrophobicity of hMSNs creates a layer of interfacial nanobubbles that isolates DOX from water. Under LIPUS, the nanobubble layer is disturbed, leading to DOX exposure to water.

LIPUS treatment also enhanced DOX intracellular accumulation. As shown in Fig. 3C, intracellular DOX fluorescence of DOX-MIMBs+LIPUS was 41.7 % and 129.3 % higher than that of free DOX and DOX-MIMBs respectively. DOX distribution was also observed. As shown in Fig. 3D, free DOX accumulated mainly in the nucleus after incubation for 2 h. However, DOX fluorescence from DOX-MIMBs was mainly distributed in the cytoplasm, indicating that DOX was not substantially released from DOX-MIMBs. As expected, after LIPUS ($0.25\ \text{W/cm}^2$, 20 s) treatment, DOX was released from DOX-MIMBs, evidenced by massive distribution in the nucleus.

LIPUS-induced internalization enhancement and LIPUS-triggered DOX release favored the antitumor efficacy of DOX-MIMBs. As shown in Fig. 3E, cell viability of DOX-MIMBs+LIPUS was lower than that of DOX-MIMBs and free DOX at all tested DOX concentrations, especially at low DOX concentrations. Specifically, at DOX concentration of $0.02\ \mu\text{g/mL}$, the cell viability of DOX-MIMBs+LIPUS was 39.8 %, while that of DOX-MIMBs and free DOX were 97.9 % and 76.4 %, respectively.

3.4. Tumor penetration of MIMBs

To evaluate tumor penetration, Renca 3D tumor spheroids were

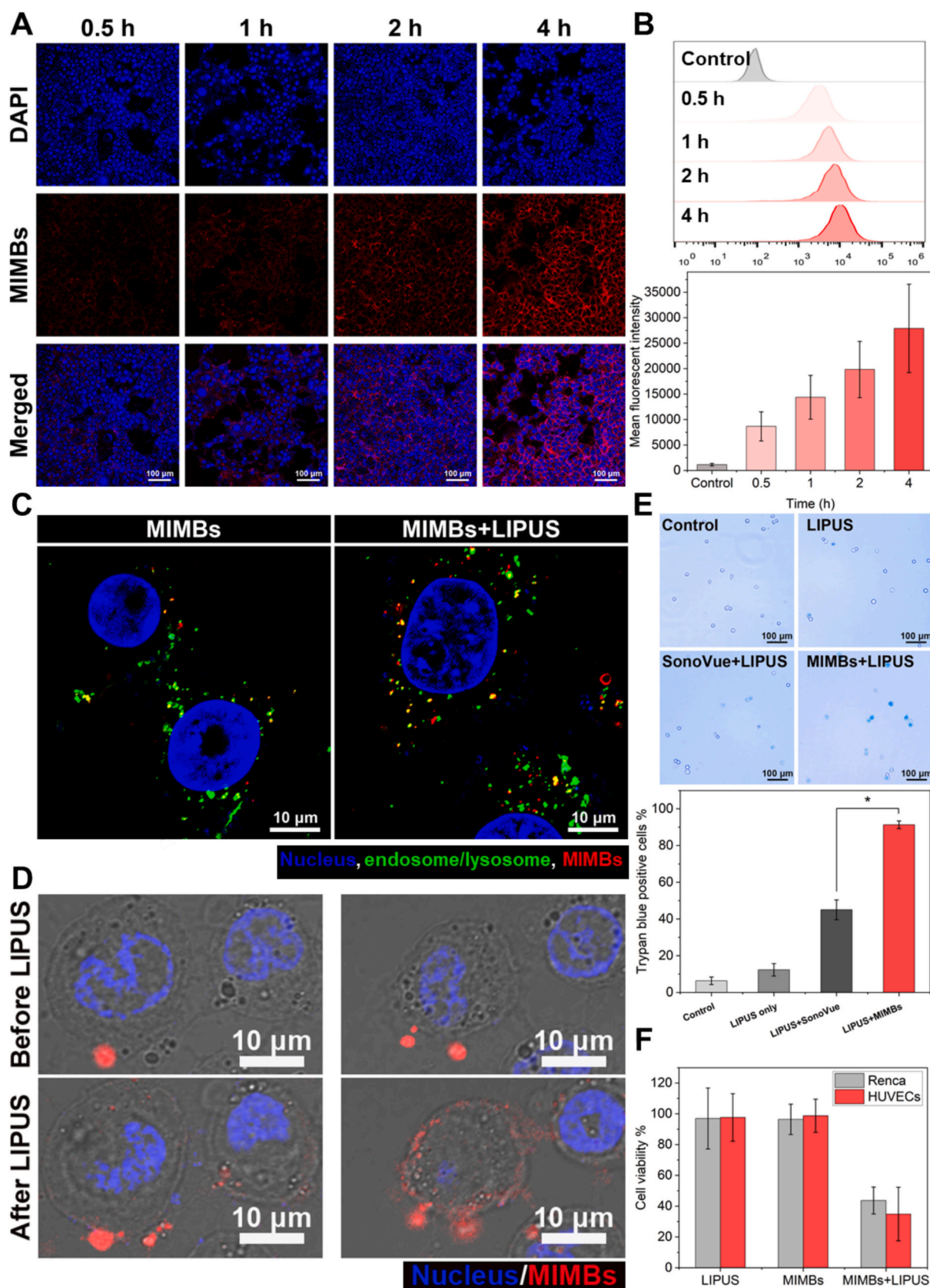


Fig. 2. (A) Confocal laser scanning microscopy (CLSM) images and (B) flow cytometry analysis of Renca cells treated with DiI-MIMBs. (C) Co-localization of DiI-MIMBs and endosomes/lysosomes in Renca cells. (D) CLSM images of Renca cells incubated with DiI-MIMBs (red) for 1 h and then treated with (0.25 W/cm², 20 s). (E) Trypan blue staining images and quantitative analysis of Renca cells treated with SonoVue and MIMB under LIPUS (0.25 W/cm², 20 s). (F) Cell viability of Renca cells and HUVECs treated with MIMBs and MIMBs+LIPUS (0.25 W/cm², 20 s). **P* < 0.05. (For interpretation of the references to color in this figure legend, the reader is referred to the web version of this article.)

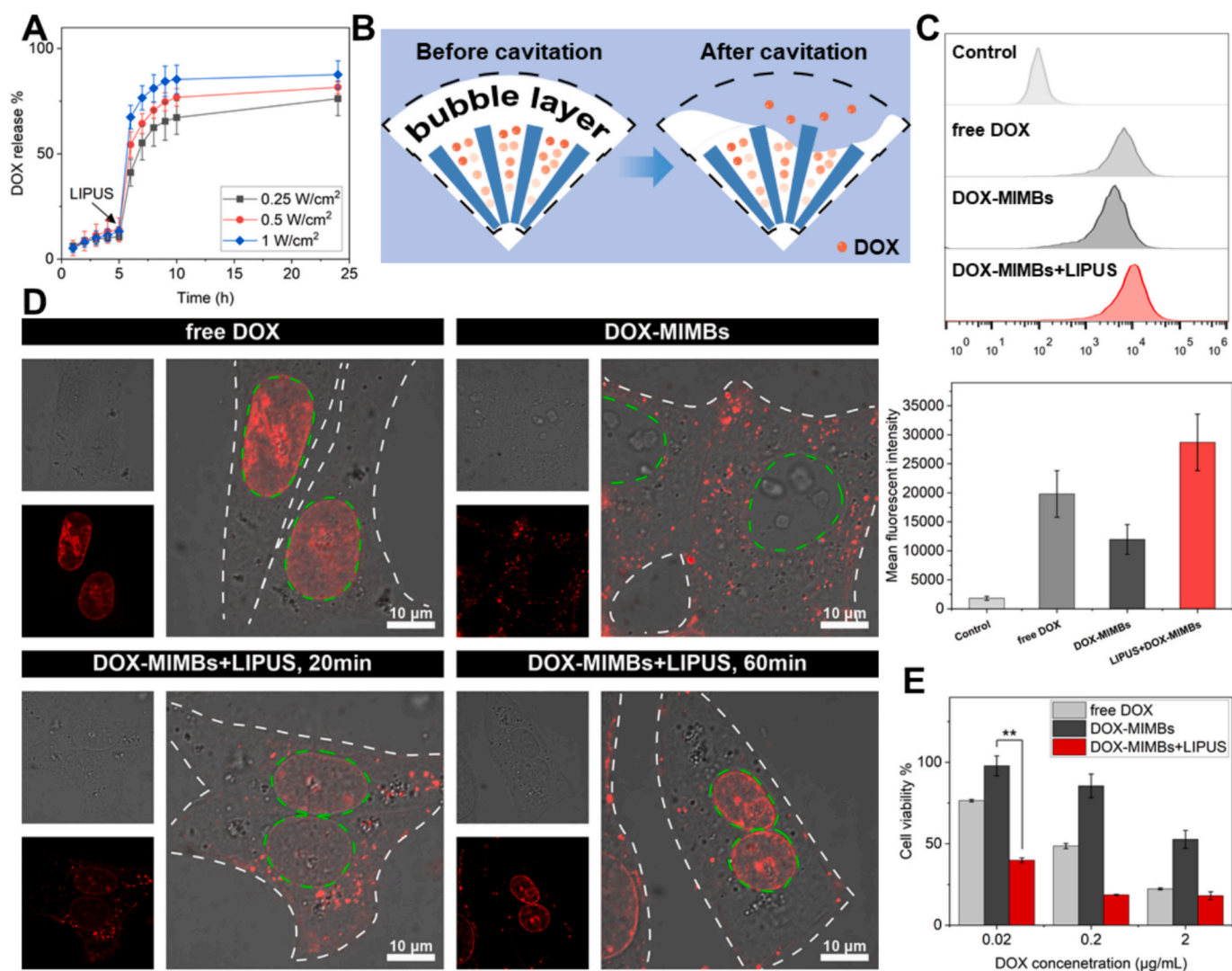


Fig. 3. (A) DOX release profile before and after LIPUS (0.25, 0.5 and 1 W/cm², 20 s) treatment. (B) Schematic diagram of LIPUS-triggered DOX release. (C) Flow cytometry analysis of Renca cells treated with free DOX, DOX-MIMBs and DOX-MIMBs+LIPUS. (D) CLSM images of Renca cells treated with free DOX, DOX-MIMBs and DOX-MIMBs+LIPUS. (E) Cell viability of Renca cells treated with free DOX, DOX-MIMBs and DOX-MIMBs+LIPUS. ***P* < 0.01.

constructed. As shown in Fig. 4A, free DOX merely outlined the spheroids with minimal penetration. Under assistance of LIPUS+SonoVue, penetration of DOX enhanced. However, as SonoVue was progressively consumed, bubble cavitation weakened, resulting in failed penetration of DOX to the core of the tumor spheroids. Interestingly, DOX-MIMBs+LIPUS achieved substantial penetration of DOX into the core of the tumor spheroids, evidenced by DOX fluorescence within the spheroid center (Fig. S7).

It is believed that enhanced and sequential MIMBs cavitation is the key for deep penetration. To evaluate the cavitation effects of MIMBs, MIMBs were treated by LIPUS (0.25 W/cm², 1 s) and the changes of ultrasound signal were observed in ultrasound imaging. As shown in Fig. 4B, the ultrasound signal of MIMBs decreased to 63.4 % after the first LIPUS (0.25 W/cm², 1 s) treatment, followed by a rapid recovery to 88.9 %. After the second LIPUS (0.25 W/cm², 1 s) treatment, the ultrasound signal of MIMBs was reduced again to 64.6 %, followed by a rapid recovery to 78.9 %. The recovery of the ultrasound signal of MIMBs after LIPUS (0.25 W/cm², 1 s) treatment indicated the formation and stabilization of daughter bubbles. However, SonoVue-derived daughter bubbles were difficult to be stabilized by phospholipids. The ultrasound signal of SonoVue decreased rapidly to 40.1 % after the first LIPUS (0.25 W/cm², 1 s) treatment, but recovered only to 51.4 %. After

the second LIPUS (0.25 W/cm², 1 s) treatment, ultrasound signal of SonoVue decreased to 36.5 % and then recovered to 41.2 %. To further demonstrate the generation and re-stabilization of daughter bubbles, bubble concentration and average size of MIMBs were examined after LIPUS (0.25 W/cm², 1 s) treatment, respectively. As shown in Fig. 4C, the concentration of MIMBs increased and the size decreased after LIPUS (0.25 W/cm², 1 s) treatment. Specifically, after LIPUS (0.25 W/cm², 1 s) treatment once, the number concentration of MIMBs increased from 5.26×10^8 per mL to 7.61×10^8 per mL (44.7 %), and the size decreased from 1.02 μm to 0.96 μm. After LIPUS (0.25 W/cm², 1 s) treatment twice, MIMBs concentration increased to 13.28×10^8 per mL (152.5 %), and the size decreased to 0.76 μm.

A hypothesis was proposed to explain the hierarchically engineered MIMBs for sequential enhanced cavitation. As depicted in Fig. 4D, LIPUS-induced MIMBs destruction produces smaller daughter bubbles. These daughter bubbles quickly re-assembled by surrounding hMSNs, generating more but smaller MIMBs. The smaller MIMBs can be cavitated again until ultrasound energy is not sufficient to initiate cavitation. However, SonoVue-derived daughter bubbles were difficult to be stabilized by phospholipids. Harnessing cavitation-induced microstreaming effects, hMSNs undergo inertial propulsion as nanobullets to achieve spatiotemporally programmed displacement from primary

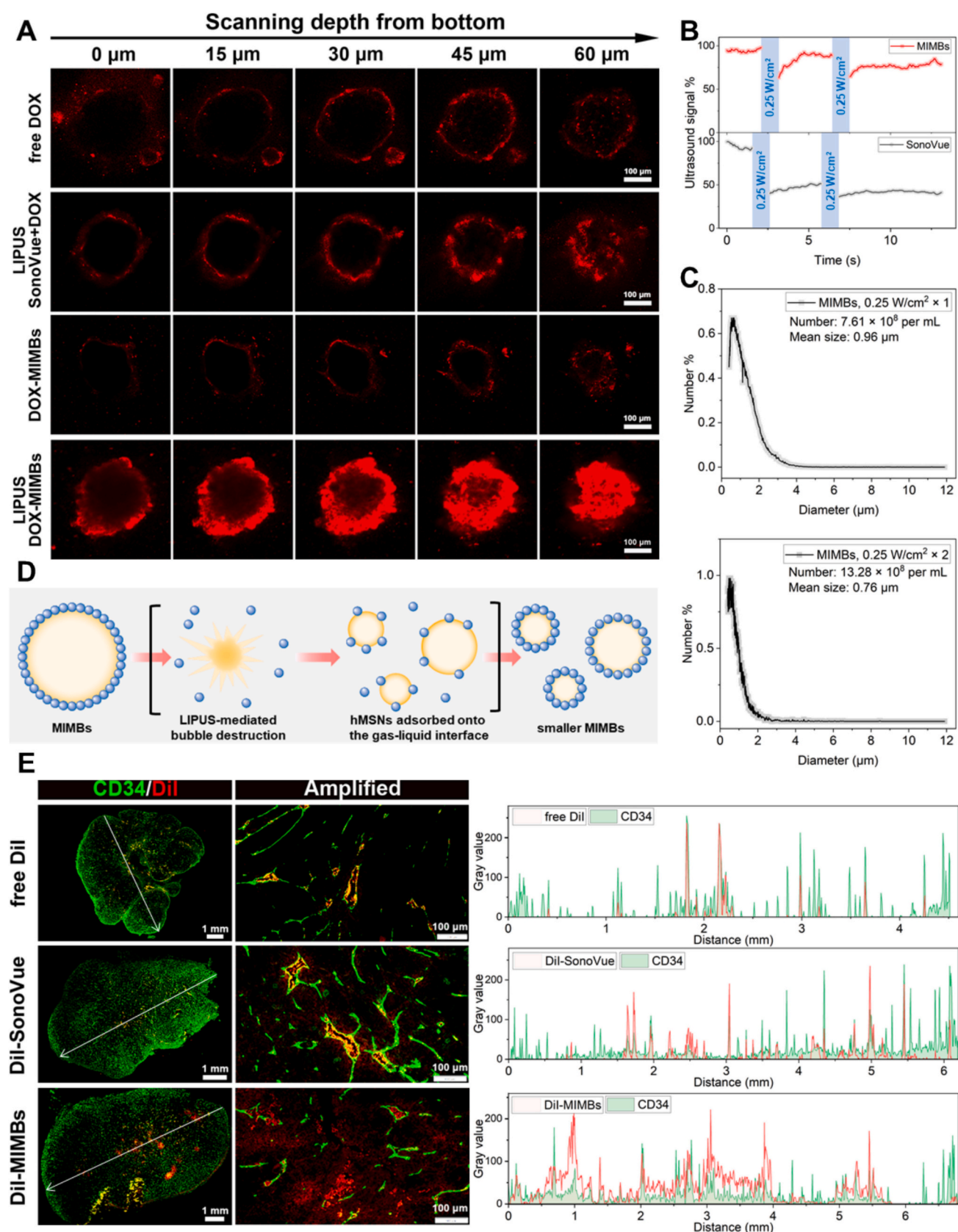


Fig. 4. (A) Fluorescent images of Renca tumor spheroids treated with free DOX, SonoVue or DOX-MIMBs with or without LIPUS treatment (0.25 W/cm^2 , 20 s). (B) Ultrasound signal changes of MIMBs and SonoVue before and after LIPUS treatment (0.25 W/cm^2 , 1 s). (C) MIMBs counting and size distribution after LIPUS treatment (0.25 W/cm^2 , 1 s) once and twice. (D) Schematic diagram of LIPUS-driven MIMBs cavitation. (E) Colocalization of CD34 (green) and free DiI, DiI-SonoVue and DiI-MIMBs (red). Co-localization curves of CD34 (green) and DiI (red) along the arrows across the tumor tissues. (For interpretation of the references to color in this figure legend, the reader is referred to the web version of this article.)

cavitation foci followed by interstitial penetration *via* secondary bubble collapse-driven momentum transfer. Therefore, enhanced MIMBs cavitation and ejected hMSNs enabled DOX-MIMBs to consistently break through the barriers while delivering DOX deep into the tumor tissue.

To further investigate the penetration effect of MIMBs *in vivo*, mice with Renca tumors were treated with DiI-MIMBs+LIPUS. Fig. 4E showed the co-localization of DiI-labeled bubbles with the tumor vasculature. Along the long axis of the tumors, free DiI + LIPUS and DiI-

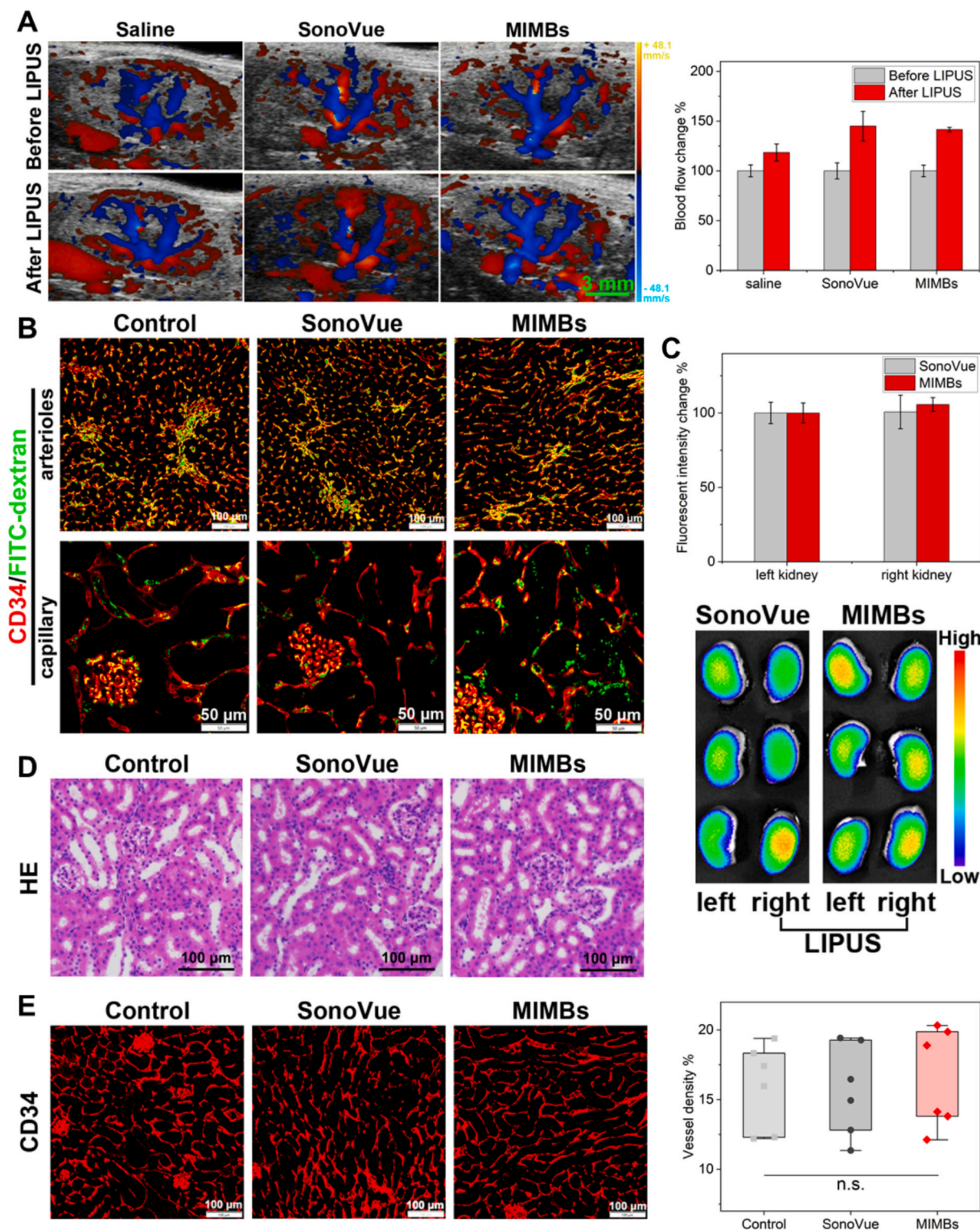


Fig. 5. (A) Color doppler images of SonoVue and MIMBs in kidneys before and after LIPUS (2 W/cm^2 , 1 min). (B) Colocalization of CD34 (red) and vessel lumen (green) in kidneys treated by SonoVue and MIMBs under LIPUS (2 W/cm^2 , 1 min). (C) Ex vivo fluorescence imaging of kidneys from mice treated with DiI-labeled SonoVue and MIMBs. After injection of DiI-labeled SonoVue and MIMBs, right kidneys were immediately treated by LIPUS (2 W/cm^2 , 1 min). (D) H&E staining of kidneys treated by SonoVue and MIMBs under LIPUS (2 W/cm^2 , 1 min). (E) CD34 vessel density of kidneys treated by SonoVue and MIMBs under LIPUS (2 W/cm^2 , 1 min). n.s., not significant. (For interpretation of the references to color in this figure legend, the reader is referred to the web version of this article.)

SonoVue+LIPUS showed a narrow distribution, while DiI-MIMBs+LIPUS exhibited a wide distribution. Compared to free DiI + LIPUS that exhibited strong co-localization with tumor vasculature (Pearsons' coefficient, 0.648), DiI-SonoVue+LIPUS exhibited weaker co-localization with tumor vasculature (Pearsons' coefficient, 0.529). Interestingly, DiI-MIMBs+LIPUS almost did not co-localized with tumor vasculature (Pearsons' coefficient, 0.240). In addition, DiI-MIMBs+LIPUS disrupted the tumor vasculature and induced vascular

incompleteness, while free DiI + LIPUS and DiI-SonoVue+LIPUS exhibited relatively intact vascular structure. These results suggested that MIMBs cavitation disrupted the tumor vasculature and facilitated drug delivery deep into the tumor tissue.

3.5. Biosafety and vascular influence

To evaluate the biosafety of LIPUS alone, kidneys were exposed to

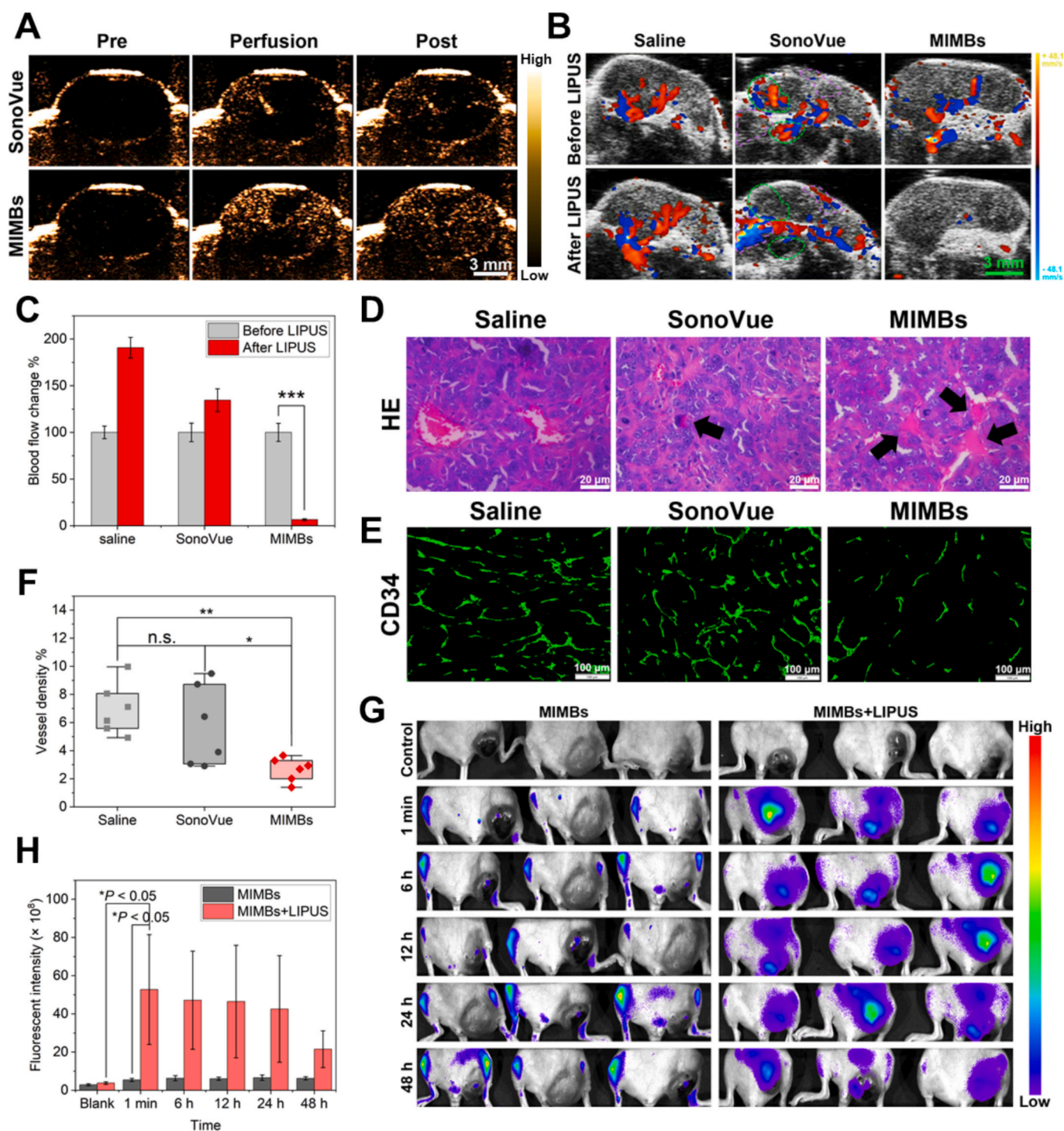


Fig. 6. (A) CEUS images of SonoVue and MIMBs in tumors. (B) Color Doppler images and (C) blood flow change of SonoVue and MIMBs in tumors before and after LIPUS (2 W/cm², 1 min). (D) H&E staining of tumors treated by SonoVue and MIMBs under LIPUS (2 W/cm², 1 min). (E) CD34 Immunofluorescence staining and (F) vessel density of tumors treated by SonoVue and MIMBs under LIPUS (2 W/cm², 1 min). (G) *In vivo* fluorescence imaging and (H) quantitative analysis of tumor-bearing mice treated with DiI-labeled MIMBs with or without LIPUS treatment (2 W/cm², 1 min). **P* < 0.05, ***P* < 0.01, ****P* < 0.001, n.s., not significant.

LIPUS with different intensities. As shown in Fig. S8, H&E staining exhibited no structural changes in glomeruli and tubules under LIPUS (1–2.5 W/cm²). Co-localization of renal blood flow (labeled with FITC-dextran, green) and vascular endothelium (CD34, red) indicated minor ruptures of peritubular capillaries (white arrows) induced by LIPUS (2.5 W/cm²). Therefore, LIPUS with 2 W/cm² was used in the following cellular experiments.

To evaluate the biosafety of MIMBs cavitation, the effect of MIMBs cavitation on renal blood flow was evaluated in healthy mouse kidneys. As shown in Fig. 5A, after LIPUS (2 W/cm², 1 min) treatment, all groups exhibited the enhanced renal perfusion overall, and no reduction or loss of blood flow was observed at any localized area. The enhanced renal perfusion could be explained by LIPUS-induced cavitation and thermal effect (Fig. S9). Both moderate cavitation and localized heating can enhance blood perfusion by stimulating endothelial nitric oxide (NO) release, reducing the contractility of the sympathetic nervous system and smooth muscle on blood vessels [39–41].

To further explore whether MIMBs cavitation disrupted renal vasculature, co-localization of renal blood flow (green) and vascular endothelium (red) was observed as shown in Fig. 5B. All FITC-dextran was observed within the arterioles, indicating intact vascular structure. However, in renal capillaries, extravasation of FITC-dextran was induced by MIMBs cavitation, while almost no extravasation could be observed by LIPUS or SonoVue cavitation. Of note, all extravasation occurred in the peritubular capillaries, which may be determined by the unique structure of peritubular capillaries. Peritubular capillaries are composed of vascular endothelium with gaps and basement membranes, which facilitates rapid exchange of substances with the renal tubules [42]. Therefore, peritubular capillaries are structurally more fragile than arterioles and glomerulus capillaries, which led to vulnerability to MIMBs cavitation.

However, it is important to emphasize that the effects of MIMBs cavitation on peritubular capillaries are transient and reversible. To begin with, MIMBs cavitation did not cause significant accumulation of MIMBs in the kidney (Fig. 5C). Next, MIMBs cavitation did not cause structural changes in the renal tubules (Fig. 5D). Finally, MIMBs cavitation also did not decrease renal cortical vascular density (Fig. 5E).

3.6. MIMBs cavitation in vivo

Tumor-bearing mice were injected with SonoVue and MIMBs via the tail vein, and tumor perfusion of bubbles was immediately observed by real-time contrast-enhanced ultrasound imaging. As shown in Fig. 6A, SonoVue lit up part of the tumor tissue, while MIMBs highlighted the entire tumor tissue. This may be due to the better performance of MIMBs over SonoVue in ultrasound imaging (Fig. S10). Besides, MIMBs (1.02 μ m) are smaller than SonoVue (~2.5 μ m). Therefore, compared to SonoVue, MIMBs were able to access smaller tumor vessels.

Tumor-bearing mice were injected with SonoVue and MIMBs, followed by immediate LIPUS (2 W/cm², 1 min) treatment. Changes of tumor blood flow were recorded and shown in Fig. 6B. Saline+LIPUS treatment enhanced tumor perfusion, which is consistent with previous reports [9]. This is mainly due to the vasodilation caused by LIPUS-induced moderate cavitation and thermal effect [39–41]. Interestingly, introduction of MIMBs extremely enhanced cavitation. As shown in Fig. 6C, MIMBs+LIPUS led to a 93.5 % reduction in overall tumor perfusion. Moreover, tumor perfusion blockade induced by MIMBs+LIPUS can last for at least 24 h, followed by gradual recovery (Fig. S11). As a comparison, SonoVue+LIPUS enhanced tumor local perfusion (purple dashed area) while only reducing perfusion (green dashed area) to other parts of the tumor.

The decrease in tumor perfusion was caused by blood clot formation, which is consistent with previous reports [43]. As shown in Fig. 6D, MIMBs+LIPUS resulted in large clot formation in tumor vasculature (black arrows), whereas SonoVue +LIPUS induced fewer clot formation. Besides, vessel density was counted as shown in Fig. 6E, F.

SonoVue+LIPUS resulted in reduction of vessel density by 17.5 %, whereas MIMBs+LIPUS resulted in its reduction by 61.8 %. Furthermore, it is interesting that the MIMBs+LIPUS group showed rapid accumulation of MIMBs in tumors. As shown in Fig. 6G, H, the fluorescence intensity of tumors in MIMBs+LIPUS group was over 9 times higher than that of MIMBs after LIPUS treatment, following by prolonged retention for at least 24 h.

Normal vasculature exhibits tightly joined endothelial cells, a continuous and intact basement membrane, which is closely enveloped by pericytes. In contrast, tumor vasculature features wide inter-endothelial gaps, a discontinuous or absent basement membrane, and sparse pericyte coverage [44], which is the structural basis of the EPR effect. Thus, this structural compromise results in tumor vessels becoming leaky and fragile, making tumor vessels more susceptible to dramatic and irreversible cavitation injury. Unlike the slow accumulation dependent on the EPR effect, LIPUS treatment caused intense cavitation of MIMBs in tumor vessels, destroying tumor vessels and increasing the transendothelial permeability of MIMBs. At the same time, MIMBs cavitation also blocked blood flow in the tumor, causing MIMBs to be trapped in the tumor tissue.

3.7. Tumor therapy efficacy

At last, the *in vivo* antitumor activity of DOX-MIMBs+LIPUS was carried out in tumor-bearing mice (Fig. 7A). Tumor volumes and body weights were recorded every two days during treatment. As shown in Fig. 7B, tumor volume of control group increased rapidly, while MIMBs+LIPUS, DOX-MIMBs and DOX-MIMBs+LIPUS were effective in inhibiting the tumor growth. Among them, DOX-MIMBs+LIPUS treatment exhibited the best antitumor efficacy. Specifically, at the end of the treatment (day 19), compared to the control group, the average tumor volumes of mice treated with DOX-MIMBs+LIPUS reduced by 89.6 %, while those of MIMBs+LIPUS and DOX-MIMBs were 42.7 % and 57.1 %, respectively. Besides, tumor weights also demonstrated the enhanced tumor inhibition of DOX-MIMBs+LIPUS. As shown in Fig. 7C, the average tumor weights in DOX-MIMBs+LIPUS group was 26.3 % and 14.4 % of that in MIMBs+LIPUS and DOX-MIMBs groups, respectively. Body weight change was a clear reflection of the systemic toxicity. As shown in Fig. 7D, MIMBs+LIPUS treatment caused 8.6 % body weight loss, while DOX-MIMBs treatment resulted in 9.0 % body weight loss. In contrast, DOX-MIMBs+LIPUS treatment did not induce any significant body weight loss, but instead increased the body weight of mice (5.0 %). These results demonstrated that DOX-MIMBs+LIPUS exhibited enhanced antitumor efficacy with minimal drug-related toxicity.

To further evaluate the antitumor efficacy of DOX-MIMBs+LIPUS, mice were sacrificed after treatment and the tumor sections were prepared and stained with CD34, H&E, TUNEL and Ki67 for pathology analysis (Fig. 7E). CD34 staining is mainly used to evaluate the existence of neovascularization. Compared to control group, CD34 expression (brown area) of MIMBs+LIPUS, DOX-MIMBs and DOX-MIMBs+LIPUS was decreased. Specifically, compared to the control group, CD34 expression was decreased by 7.9 %, 4.8 % and 21.1 % by MIMBs+LIPUS, DOX-MIMBs and DOX-MIMBs+LIPUS, respectively (Fig. 7F). It is important to emphasize that, unlike conventional anti-angiogenesis strategies that rely on drugs or compounds targeting the VEGF/VEGFR pathway, MIMBs inhibit tumor neovascularization through violent mechanical disruption.

Pathology analysis further showed that H&E-stained tumor sections from the untreated control group exhibited typical malignant features, including cells with large, spherical or spindle shaped nuclei and increased chromatin content. After different treatments, necrotic cells were observed (white dotted area), exhibiting unclear cell morphology and dark chromatin. Among them, DOX-MIMBs+LIPUS caused a larger area of tumor necrosis than MIMBs+LIPUS and DOX-MIMBs, suggesting better antitumor activity of DOX-MIMBs+LIPUS. TUNEL and Ki67 staining of tumor tissues also supported the enhanced antitumor

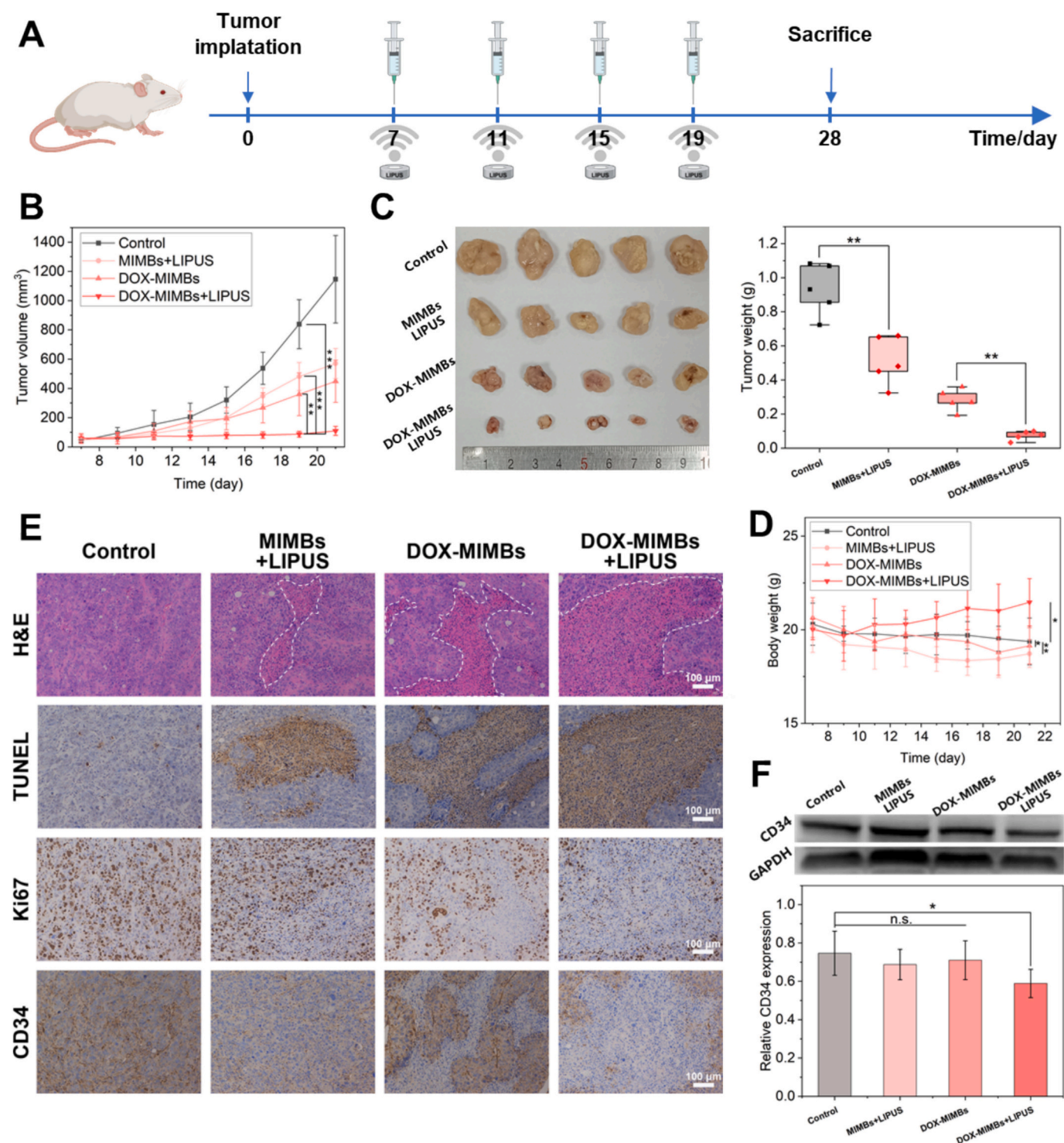


Fig. 7. (A) Protocol of tumor therapy with DOX-MIMBs+LIPUS in Renca tumor-bearing mice. (B) Tumor growth curves of mice after various treatments ($n = 5$). (C) Images and tumor weights of separated tumor tissues after treatment. (D) Body weights of mice during treatments. (E) H&E, TUNEL, Ki67 and CD34 staining of tumors from mice after different treatments. (F) CD34 expression of tumors after different treatments. * $P < 0.05$, ** $P < 0.01$, *** $P < 0.001$, n.s., not significant.

performance of DOX-MIMBs+LIPUS. Compared with MIMBs+LIPUS and DOX-MIMBs groups, better apoptosis induction and proliferation inhibition were achieved by DOX-MIMBs+LIPUS, demonstrating a higher antitumor efficacy. Besides, no obvious pathological damage was observed in major organs after treatment of DOX-MIMBs+LIPUS (Fig. S12).

4. Conclusion

In summary, MIMBs are multi-interfacial microbubbles by nature and exhibit unique stability and ultrasound responsiveness different from that of conventional gas-encapsulated microbubbles. While the daughter bubbles generated by conventional bubbles dissipate rapidly after the initial cavitation, the daughter bubbles generated by MIMBs can be rapidly re-stabilized by hMSNs due to the affinity of the

hydrophobic surface for the gas-liquid interface, thus exhibiting sustained cavitation. Meanwhile, the sequential cavitation induced microstreaming mechanical force propels hMSNs like nanobubbles to be ejected multiple times, thus penetrating deep into the tumor tissue. Under LIPUS, MIMBs disrupted tumor blood vessels and blocked tumor blood perfusion. MIMBs cavitation also decreased tumor vessel density and broke through barriers to delivery DOX deep into tumor tissues. In addition, MIMBs cavitation exhibits tumor specificity with minimal damage to normal organs. Such elaborated MIMBs achieve a paradigm shift from systemic drug bombardment to local mechanochemical tumor suppression and provide a powerful strategy for tumor therapy.

CRedit authorship contribution statement

Tiandong Chen: Writing – review & editing, Writing – original draft, Visualization, Validation, Methodology, Investigation, Conceptualization. **Chenyi Zhang:** Methodology, Investigation. **Yanxiao Zhao:** Methodology. **Yakun Wang:** Investigation. **Mingxi Li:** Validation, Methodology. **Yang Liu:** Investigation. **Xiao Wang:** Validation. **Shuangyu Liu:** Methodology. **Dan Mu:** Supervision, Resources. **Fang Yang:** Writing – review & editing, Writing – original draft, Supervision, Project administration, Methodology, Funding acquisition, Conceptualization.

Declaration of competing interest

The authors declare no competing interests.

Acknowledgements

This investigation was financially funded by the National Key Research and Development Program of China (2023YFF0713600), the Natural Science Foundation of Jiangsu Province (BK20222002), and Project 333 of Jiangsu Province.

Appendix A. Supplementary data

Supplementary data to this article can be found online at <https://doi.org/10.1016/j.jconrel.2025.114287>.

Data availability

All data needed to evaluate the conclusions in the paper are present in the Article. Additional data are available from the corresponding author upon reasonable request.

References

- M.A. Alhammedi, K. Bajbouj, I.M. Talaat, R. Hamoudi, The role of RNA-modifying proteins in renal cell carcinoma, *Cell Death Dis.* 15 (2024) 227, <https://doi.org/10.1038/s41419-024-06479-y>.
- L. Lei, K. Wang, Synergistic combination of an intelligent nanozyme and radiotherapy for treating renal cancer, *Int. J. Nanomedicine* 19 (2024) 699–707, <https://doi.org/10.2147/IJN.S415668>.
- D. Liang, S. Yang, Z. Ding, X. Xu, W. Tang, Y. Wang, K. Qian, Engineering a bifunctional smart nanoplatform integrating nanozyme activity and self-assembly for kidney cancer diagnosis and classification, *ACS Nano* 18 (2024) 23625–23636, <https://doi.org/10.1021/acsnano.4c08085>.
- S. Yoodee, P. Peerapen, S. Plumworasawat, T. Malaitad, V. Thongboonkerd, Identification and characterization of ARID1A-interacting proteins in renal tubular cells and their molecular regulation of angiogenesis, *J. Transl. Med.* 21 (2023) 1–22, <https://doi.org/10.1186/s12967-023-04750-y>.
- Z.L. Liu, H.H. Chen, L.L. Zheng, L.P. Sun, L. Shi, Angiogenic signaling pathways and anti-angiogenic therapy for cancer, *Signal Transduct. Target. Ther.* 8 (2023) 1–39, <https://doi.org/10.1038/s41392-023-01460-1>.
- C. Song, X. Guan, C. Xie, S. Jiang, Z. Hong, Q. Wu, G. Qu, T. Ma, Y. Cui, Inhibiting PI3K/AKT/mTOR signaling by metal-organic frameworks for overcoming multiple drug resistance in chemoradiotherapy, *Sci. China Mater.* 67 (2024) 1631–1645, <https://doi.org/10.1007/s40843-023-2774-8>.
- D. Li, F. Shao, Q. Yu, R. Wu, Z. Tuo, J. Wang, L. Ye, Y. Guo, K.H. Yoo, M. Ke, U. A. Okoli, C. Premkamon, Y. Yang, W. Wei, S. Heavey, W.C. Cho, D. Feng, The complex interplay of tumor-infiltrating cells in driving therapeutic resistance pathways, *Cell Commun. Signal* 22 (2024) 405, <https://doi.org/10.1186/s12964-024-01776-7>.
- Y. Han, J. Sun, H. Wei, J. Hao, W. Liu, X. Wang, Ultrasound-targeted microbubble destruction: modulation in the tumor microenvironment and application in tumor immunotherapy, *Front. Immunol.* 13 (2022) 1–12, <https://doi.org/10.3389/fimmu.2022.937344>.
- D. Qiu, Y. He, Y. Feng, M. Lin, Z. Lin, Z. Zhang, Y. Xiong, Z. Hu, S. Ma, H. Jin, J. Liu, Tumor perfusion enhancement by microbubbles ultrasonic cavitation reduces tumor glycolysis metabolism and alleviate tumor acidosis, *Front. Oncol.* 14 (2024) 1–13, <https://doi.org/10.3389/fonc.2024.1424824>.
- C.W. Lin, C.H. Fan, C.K. Yeh, The relationship between surface drug distribution of Dox-loaded microbubbles and drug release/cavitation behaviors with ultrasound, *Ultrason. Sonochem.* 102 (2024) 106728, <https://doi.org/10.1016/j.ultrasonch.2023.106728>.
- C. Pellow, A. Jafari Sojahrood, X. Zhao, M.C. Kolios, A.A. Exner, D.E. Goertz, Synchronous intravital imaging and cavitation monitoring of antivasculature focused ultrasound in tumor microvasculature using monodisperse low boiling point nanodroplets, *ACS Nano* 18 (2024) 410–427, <https://doi.org/10.1021/acsnano.3c07711>.
- Y. Li, Z. Gao, X. Zheng, Y. Pan, J. Xu, Y. Li, H. Chen, Interventional removal of travelling microthrombi using targeted magnetic microbubble, *Adv. Healthc. Mater.* 2401631 (2024) 1–11, <https://doi.org/10.1002/adhm.202401631>.
- A.D. Jose, Z. Wu, S.S. Thakur, A comprehensive update of micro- and nanobubbles as therapeutics in oncology, *Eur. J. Pharm. Biopharm.* 172 (2022) 123–133, <https://doi.org/10.1016/j.ejpb.2022.02.008>.
- C. He, Z. Wu, M. Zhuang, X. Li, S. Xue, S. Xu, J. Xu, Z. Wu, M. Lu, Focused ultrasound-mediated blood-brain barrier opening combined with magnetic targeting cytomembrane based biomimetic microbubbles for glioblastoma therapy, *J. Nanobiotechnol.* 21 (2023) 1–12, <https://doi.org/10.1186/s12951-023-02074-z>.
- Y. Wu, T. Sun, J. Tang, Y. Liu, F. Li, Ultrasound-targeted microbubble destruction enhances the antitumor efficacy of doxorubicin in a mouse hepatocellular carcinoma model, *Ultrasound Med. Biol.* 46 (2020) 679–689, <https://doi.org/10.1016/j.ultrasmedbio.2019.09.017>.
- J. Yu, K. Hu, Z. Zhang, L. Luo, Y. Liu, D. Zhou, F. Wang, Y. Kuang, H. Xu, H. Li, H. Duan, X. Sun, Interfacial nanobubbles' growth at the initial stage of electrocatalytic hydrogen evolution, *Energ. Environ. Sci.* 16 (2023) 2683–2687, <https://doi.org/10.1039/d2ee04143j>.
- Y. Jonosono, S.I. Tsuda, T. Tokumasu, H. Nagashima, Molecular dynamics study of the microscopic mechanical balance at the three-phase contact line of interfacial nanobubble, *Langmuir* 40 (2024) 8440–8449, <https://doi.org/10.1021/acs.langmuir.3c04027>.
- H. Yang, E. Ding, F. Zhang, Y. Xing, X. Gui, Y. Cao, The stability and geometrical characteristics of solid-liquid interfacial nanobubbles in complex aqueous solution environments, *Surf Interfaces* 46 (2024) 104027, <https://doi.org/10.1016/j.surf.2024.104027>.
- R. Xiong, R.X. Xu, C. Huang, S. De Smedt, K. Braeckmans, Stimuli-responsive nanobubbles for biomedical applications, *Chem. Soc. Rev.* 50 (2021) 5746–5776, <https://doi.org/10.1039/c9cs00839j>.
- A. Upadhyay, S.V. Dalvi, Microbubble formulations: synthesis, stability, modeling and biomedical applications, *Ultrasound Med. Biol.* 45 (2019) 301–343, <https://doi.org/10.1016/j.ultrasmedbio.2018.09.022>.
- T. Maruyama, M. Sugii, D. Omata, J. Unga, T. Shima, L. Munakata, S. Kageyama, F. Hagiwara, Y. Suzuki, K. Maruyama, R. Suzuki, Effect of lipid shell composition in DSPG-based microbubbles on blood flow imaging with ultrasonography, *Int. J. Pharm.* 590 (2020) 119886, <https://doi.org/10.1016/j.ijpharm.2020.119886>.
- Y. Liu, X. Zhang, Evaporation dynamics of nanodroplets and their anomalous stability on rough substrates, *Phys. Rev. E - Stat. Nonlinear, Soft Matter Phys.* 88 (2013) 1–6, <https://doi.org/10.1103/PhysRevE.88.012404>.
- J. Wei, X. Zhang, F. Song, Deformation of surface nanobubbles induced by substrate hydrophobicity, *Langmuir* 32 (2016) 13003–13008, <https://doi.org/10.1021/acs.langmuir.6b03236>.
- Z. Xu, H. Liu, H. Tian, F. Yan, Real-time imaging tracking of engineered macrophages as ultrasound-triggered cell bombs for cancer treatment, *Adv. Funct. Mater.* 30 (2020) 1–10, <https://doi.org/10.1002/adfm.201910304>.
- Y. Huang, K. Shen, Y. Si, C. Shan, H. Guo, M. Chen, L. Wu, Dendritic organosilica nanospheres with large mesopores as multi-guests vehicle for photoacoustic/ultrasound imaging-guided photodynamic therapy, *J. Colloid Interface Sci.* 583 (2021) 166–177, <https://doi.org/10.1016/j.jcis.2020.09.028>.
- J. Zhang, T. Guo, K. Liu, K. Bao, X. Liu, S. Cui, D. Chen, M.J. Li, S. Bao, C. Hu, X. Wei, X. Gao, Ultrasonic diagnosis and treatment of tumors using multifunctional hollow mesoporous silicon nanoparticles, *ACS Appl. Nano Mater.* 7 (2024) 15446–15458, <https://doi.org/10.1021/acsnano.4c02319>.
- Q. Zhao, Y. Yang, H. Wang, W. Lei, Y. Liu, S. Wang, Gold nanoparticles modified hollow carbon system for dual-responsive release and chemo-photothermal synergistic therapy of tumor, *J. Colloid Interface Sci.* 554 (2019) 239–249, <https://doi.org/10.1016/j.jcis.2019.07.005>.
- S. Feng, Y. Mao, X. Wang, M. Zhou, H. Lu, Q. Zhao, S. Wang, Triple stimuli-responsive ZnO quantum dots-conjugated hollow mesoporous carbon nanoplatform for NIR-induced dual model antitumor therapy, *J. Colloid Interface Sci.* 559 (2020) 51–64, <https://doi.org/10.1016/j.jcis.2019.09.120>.
- Q. Zhao, S. Wang, Y. Yang, X. Li, D. Di, C. Zhang, T. Jiang, S. Wang, Hyaluronic acid and carbon dots-gated hollow mesoporous silica for redox and enzyme-triggered targeted drug delivery and bioimaging, *Mater. Sci. Eng. C* 78 (2017) 475–484, <https://doi.org/10.1016/j.msec.2017.04.059>.

- [30] J. Montoya Mira, L. Wu, S. Sabuncu, A. Sapre, F. Civitci, S. Ibsen, S. Esener, A. Yildirim, Gas-stabilizing sub-100 nm mesoporous silica nanoparticles for ultrasound theranostics, *ACS Omega* 5 (2020) 24762–24772, <https://doi.org/10.1021/acsomega.0c03377>.
- [31] Y.J. Ho, C.H. Wu, Q. feng Jin, C.Y. Lin, P.H. Chiang, N. Wu, C.H. Fan, C.M. Yang, C. K. Yeh, Superhydrophobic drug-loaded mesoporous silica nanoparticles capped with β -cyclodextrin for ultrasound image-guided combined antivasculature and chemo-sonodynamic therapy, *Biomaterials* 232 (2020) 119723, <https://doi.org/10.1016/j.biomaterials.2019.119723>.
- [32] O. Hamzaoui, X. Monnet, J.L. Teboul, Pulsus paradoxus, *Eur. Respir. J.* 42 (2013) 1696–1705, <https://doi.org/10.1183/09031936.00138912>.
- [33] S. Magder, Heart-lung interaction in spontaneous breathing subjects: the basics, *Ann. Transl. Med.* 6 (2018) 348, <https://doi.org/10.21037/atm.2018.06.19>.
- [34] Z. Xin, G. Lin, H. Lei, T.F. Lue, Y. Guo, Clinical applications of low-intensity pulsed ultrasound and its potential role in urology, *Transl. Androl. Urol.* 5 (2016) 255–266, <https://doi.org/10.21037/tau.2016.02.04>.
- [35] S. Mathlouthi, L. Kuryk, M. Prygiel, M.G. Lupo, A.A. Zasada, C. Pesce, N. Ferri, B. Rinner, S. Salmaso, M. Garofalo, Extracellular vesicles powered cancer immunotherapy: targeted delivery of adenovirus-based cancer vaccine in humanized melanoma model, *J. Control. Release* 376 (2024) 777–793, <https://doi.org/10.1016/j.jconrel.2024.10.057>.
- [36] Y.X. Chen, Y.L. Chen, T.H. Yen, Investigating interfacial effects on surface nanobubbles without pinning using molecular dynamics simulation, *Langmuir* 34 (2018) 15360–15369, <https://doi.org/10.1021/acs.langmuir.8b03016>.
- [37] D. Li, Y. Ji, Z. Wei, L. Wang, Toward a comprehensive understanding of the anomalously small contact angle of surface nanobubbles, *Langmuir* 40 (2024) 8721–8729, <https://doi.org/10.1021/acs.langmuir.4c00609>.
- [38] X. Zhang, M.H. Uddin, H. Yang, G. Toikka, W. Ducker, N. Maeda, Effects of surfactants on the formation and the stability of interfacial nanobubbles, *Langmuir* 28 (2012) 10471–10477, <https://doi.org/10.1021/la301851g>.
- [39] Y. Xiang, L. Tang, H. Pang, H. Xu, Y. He, Y. Feng, L. Ju, L. Zhang, D. Wang, Ultrasound-induced thermal effect enhances the efficacy of chemotherapy and immunotherapy in tumor treatment, *Int. J. Nanomedicine* 19 (2024) 6677–6692, <https://doi.org/10.2147/IJN.S464830>.
- [40] M.S. Karthikesh, X. Yang, The effect of ultrasound cavitation on endothelial cells, *Exp. Biol. Med.* 246 (2021) 758–770, <https://doi.org/10.1177/1535370220982301>.
- [41] K. Sriram, J.G. Laughlin, P. Rangamani, D.M. Tartakovsky, Shear-induced nitric oxide production by endothelial cells, *Biophys. J.* 111 (2016) 208–221, <https://doi.org/10.1016/j.bpj.2016.05.034>.
- [42] S. Fleischer, D.N. Tavakol, G. Vunjak-Novakovic, From arteries to capillaries: approaches to engineering human vasculature, *Adv. Funct. Mater.* 30 (2020) 1–23, <https://doi.org/10.1002/adfm.201910811>.
- [43] Z. Liu, S. Gao, Y. Zhao, P. Li, J. Liu, P. Li, K. Tan, F. Xie, Disruption of tumor neovasculature by microbubble enhanced ultrasound: a potential new physical therapy of anti-angiogenesis, *Ultrasound Med. Biol.* 38 (2012) 253–261, <https://doi.org/10.1016/j.ultrasmedbio.2011.11.007>.
- [44] R. Hultborn, L. Weiss, E. Tveit, S. Lange, E. Jennische, M.C. Erlandsson, M. E. Johansson, Ex vivo vascular imaging and perfusion studies of normal kidney and tumor vasculature, *Cancers* 16 (2024) 1939, <https://doi.org/10.3390/cancers16101939>.